© Springer-Verlag 2002

ORIGINAL PAPER

J. Majzlan · A. Navrotsky · B. J. Evans

Thermodynamics and crystal chemistry of the hematite–corundum solid solution and the FeAlO₃ phase

Abstract High-temperature oxide-melt calorimetry and Rietveld refinement of powder X-ray diffraction patterns were used to investigate the energetics and structure of the hematite–corundum solid solution and ternary phase $FeAlO_3$ (with $FeGaO_3$ structure). The mixing enthalpies in the solid solution can be described by a polynomial $\Delta H_{mix} = WX_{hem}(1-X_{hem})$ with $W = 116 \pm 10$ kJ mol^{-1}. The excess mixing enthalpies are too positive to reproduce the experimental phase diagram, and excess entropies in the solid solution should be considered. The hematite–corundum solvus can be approximately reproduced by a symmetric, regular-like solution model with $\Delta G_{excess} = (W_H - TW_S)X_{hem}X_{cor}$, where $W_H = 116 \pm 10$ kJ mol^{-1} and $W_S = 32 \pm 4$ J mol^{-1} K^{-1}. In this model, short-range order (SRO) of Fe/Al is neglected because SRO probably becomes important only at intermediate compositions close to Fe:Al = 1:1 but these compositions cannot be synthesized. The volume of mixing is positive for Al-hematite but almost ideal for Fe-corundum. Moreover, the degree of deviation from Vegard's law for Al-hematite depends on the history of the samples. Introduction of Al into the hematite structure causes varying distortion of the hexagonal network of oxygen ions while the position of the metal ions remains intact. Distortion of the hexagonal network of oxygen ions attains a minimum at the composition $(Fe_{0.95}Al_{0.05})_2O_3$. The enthalpy of formation of $FeAlO_3$ from oxides at 298 K is 27.9 ± 1.8 kJ mol^{-1}. Its estimated standard entropy (including configurational entropy due to disorder of Fe/Al) is 98.9 J mol^{-1} K^{-1}, giving the standard free energy of formation at 298 K from oxides and elements as $+19.1 \pm 1.8$ and -1144.2 ± 2.0 kJ mol^{-1}, respectively. The heat capacity of $FeAlO_3$ is approximated as $C_p(T$ in K$) = 175.8 - 0.002472T - (1.958 \times 10^6)/T^2 - 917.3/T^{0.5} + (7.546 \times 10^{-6})T^2$ between 298 and 1550 K, based on differential scanning calorimetric measurements. No ferrous iron was detected in $FeAlO_3$ by Mössbauer spectroscopy. The ternary phase is entropy stabilized and is predicted to be stable above about 1730 ± 70 K, in good agreement with the experiment. Static lattice calculations show that the LiNbO₃-, FeGaO₃-, FeTiO₃-, and disordered corundum-like $FeAlO_3$ structures are less stable (in the order in which they are listed) than a mechanical mixture of corundum and hematite. At high temperatures, the FeGaO₃-like structure is favored by its entropy, and its stability field appears on the phase diagram.

J. Majzlan (✉) · A. Navrotsky
Thermochemistry Facility
Department of Geology
University of California at Davis
Davis California 95616, USA
e-mail: jmajzlan@ucdavis.edu
Fax: +1-530-752-9307
Tel.: +1-530-754-2131

B. J. Evans
Department of Chemistry
University of Michigan
Ann Arbor Michigan 48109, USA

Introduction

It is important to understand the geochemical similarities and differences between ferric iron and aluminum. Both elements are commonly incorporated in minerals and dissolved in natural waters (Anovitz et al. 1991; Cornell and Schwertmann 1996). Solid Fe^{3+} and Al^{3+} phases exhibit extensive polymorphism with a number of isostructural compounds. On the other hand, there are also crystal structures of iron oxides (e.g., akaganeite) and structures of aluminum oxides (e.g., gibbsite) that have no isostructural counterpart with the other metal, although some Al substitution in the akageneite structure has been reported (Cheng et al. 2001). Some of the solid solutions between isostructural Fe and Al end members appear to be continuous (jarosite–alunite,

Stoffregen et al. 2000); in others the solubility is limited (hematite–corundum, goethite–diaspore, Cornell and Schwertmann 1996).

Hematite (α-Fe_2O_3) is abundant in soils and sediments (Cornell and Schwertmann 1996), and aluminum is the most common substituent in its crystal structure. The hematite–corundum solid solution was studied by Schwertmann et al. (1979), Barron et al. (1984), De Grave et al. (1988), and others (see Cornell and Schwertmann 1996 for more references). The experimental techniques employed in these studies included X-ray diffraction, infrared spectroscopy, transmission electron microscopy, thermal analysis, Mössbauer spectroscopy, and EXAFS. Mongelli and Acquafredda (1999) analyzed ferruginous concretions from Italian karst bauxites and found that they consist of Al-hematite (average composition $Fe_{0.88}Al_{0.12}O_{1.5}$) and boehmite. Grubb (1971) and Wells et al. (1989) addressed the occurrence and origin of corundum and Al-hematite in bauxitic rocks.

Mixtures of hematite and corundum are also encountered in industrial applications. Addition of Fe^{3+} to Al_2O_3 precursors may enhance nucleation kinetics and preserve nanocrystalline features of corundum ceramics (Polli et al. 1996). Fe_2O_3/Al_2O_3 assemblies find their use in catalysis for the reduction of NO_x in flue gases (Willey et al. 1991) and oxidation of CO and C_2H_4 in automotive exhaust gases (Walker et al. 1988). Al_2O_3-rich scales (with corundum structure) are a common corrosion product of Fe–Al–Cr alloys (e.g., Stott et al. 1998).

In this study, we investigated the thermochemistry and crystal chemistry of the hematite–corundum solid solution series and the ternary phase $FeAlO_3$. Measured enthalpies of formation and heat capacity were combined with the phase diagram of Muan and Gee (1956) to present a full thermodynamic description of the solid solution and the ternary phase. The experimental calorimetric data are supported by static lattice calculations. In addition, the calculations allow assessment of the energetics of ordered $FeAlO_3$ phases which cannot be synthesized and were not found in nature. The crystallographic data are used to explain previous observations of Schwertmann et al. (1979) and De Grave et al. (1988).

Experimental procedures

Sample synthesis

The hematite–corundum solid solution samples and $FeAlO_3$ (AL-1.6 through AL-1.18) were prepared by mixing appropriate proportions of reagent grade ferric and aluminum nitrate nonahydrate. The mixture was dissolved in deionized water and heated to boil off the water rapidly. The rusty residuum was gently ground, pressed into $\sim$1 g pellets and preannealed at 673 K for 4 h. The pellets were then annealed at chosen temperatures (1623 K for hematite-rich samples, 1673 K for corundum-rich samples) in a vertical Deltech furnace. The thermocouple was calibrated against the melting point of pure gold (1337 K). The temperature was controlled within

$\pm$ 5 K of the preset value. Two days of annealing were sufficient to produce a coarse well-crystalline product. The samples were quenched in water and dried in vacuum at room temperature. These samples will be referred to as the high-temperature hematite–corundum samples.

Another set of Al-hematite samples was prepared by thermal decomposition of Al-goethite at 975 K overnight. The goethite samples were synthesized by following the procedure described by Schwertmann and Cornell (2000). Characterization, thermodynamics, and crystal chemistry of these goethite samples will be the subject of a separate contribution. In this study, only the Al-hematite samples derived from these Al-goethite preparations have been studied, and are referred to as low-temperature Al-hematite samples.

Chemical analysis

The high-temperature hematite–corundum samples were mounted for optical and electron microprobe examination. We found that optical microscopy in reflected polarized light is more sensitive to impurities than X-ray diffraction. The samples were polished only with diamond pastes to avoid contamination of the surface layer with Al from Al_2O_3-based abrasives. Electron microprobe analyses were performed with a Cameca SX-50 electron microprobe, with an accelerating voltage of 15 kV, a current of 10 nA, a beam size of 5 μm, and counting time of 10 s for each analyte, with synthetic corundum and hematite as the standards.

Low-temperature Al-hematite samples were analyzed by electron microprobe although it was much more difficult to obtain good analyses owing to poor polish of the fine powder. The precursor Al-goethite samples were analyzed for Fe and Al by ICP-AAS, and the results of the two analytical techniques were in good agreement.

Water content of low-T Al-hematite was determined by heating the samples at 1180 K in corundum crucibles overnight because Gualtieri and Venturelli (1999) have shown that hematite loses all excess (adsorbed and structural) water by firing at > 1080 K. Repeated firing of empty corundum crucibles showed that an error of $\pm$ 0.03 mg is associated with the procedure. Approximately 20 mg of sample was used in each experiment, and the samples lost at least 0.07 mg upon firing, well outside the random error quoted above.

X-ray diffraction (XRD)

XRD patterns were collected with a Scintag PAD V diffractometer (Cu Kα radiation) with a diffracted beam graphite monochromator. The high-T hematite samples were ground in a McCrone micronizing mill to particle size 1–10 μm. The milling time was 2 min, as determined by particle-size measurement of a milled hematite sample using a laser-scattering particle-size distribution analyzer (Horiba LA-910). Only one corundum sample was milled to minimize abrasion load on the plastic grinding jar and agate cylinders. The low-T Al-hematite samples were not milled as they are sufficiently fine-grained. Milling significantly improves the fit of the peak shape and intensities of the X-ray lines, but the position of the XRD peaks does not shift. The lattice parameters derived from the XRD patterns of the ground and unground sample are equal. The samples were backloaded on a frosted glass slide to minimize preferred orientation. GSAS software (Larson and von Dreele 1994) was used to calculate the lattice parameters (and atomic positions and site occupancies for selected samples) by Rietveld refinement. Starting models for the Rietveld refinement were taken from Finger and Hazen (1978) for corundum, Blake et al. (1966) for hematite, and Bouree et al. (1996) for $FeAlO_3$.

High-temperature calorimetry

The enthalpy changes of interest were measured by high-temperature oxide-melt solution calorimetry (Navrotsky 1997). This technique was selected because of the ease of dissolution of corundum

and hematite in the calorimetric solvent (lead borate, $2PbO \cdot B_2O_3$ at 975 or 1075 K). The calorimeter was calibrated by dropping ~5 mg pellets of corundum (99.997% metals basis, Alfa Aesar) into an empty crucible and relating the integrated signal to the known heat content. Prior to the calibration, the Al_2O_3 powder was annealed at 1773 K overnight to remove trace moisture and ensure full conversion to corundum. Three types of high-temperature calorimetry experiments are possible. Dropping a pellet of a sample into an empty platinum crucible at temperature T gives the heat content, H_T-H_{298}. Samples can be also equilibrated over the calorimetric solvent and dissolved at calorimeter temperature T, giving the heat of solution $\Delta H_{sol,T}$. The sum of heat content and heat of solution can be measured directly by dropping the sample from room temperature into the molten solvent, giving heat of drop solution $\Delta H_{dsol,T}$ at temperature T. Because enthalpy is a state function, $(H_T$-$H_{298}) + \Delta H_{sol,T} = \Delta H_{dsol,T}$. This relation was used for derivation of thermochemical properties of low-T Al-hematite samples. This relation can also be used to check the accuracy of calorimetry because the sum of $(H_T$-$H_{298})$, $\Delta H_{sol,T}$, and $-\Delta H_{dsol,T}$ represents a circular integral of dH, zero by definition. The $(H_T$-$H_{298})$, $\Delta H_{sol,T}$, and $\Delta H_{dsol,T}$ for corundum at 975 K are 74.90, 34.53 ± 1.47, and 108.46 ± 0.60 kJ mol^{-1}, and for hematite at 975 K 96.86 ± 0.45, 73.94 ± 2.74, and 170.59 ± 1.29 kJ mol^{-1}, respectively. These values give the circular integral of $-1.0 ± 1.6$ kJ mol^{-1} for corundum and $-0.2 ± 3.1$ kJ mol^{-1} for hematite, thus documenting good accuracy of the calorimetric procedure. The $(H_T$-$H_{298})$ value for corundum was calculated by integrating the tabulated heat capacity of corundum rather than experimental measurement because this value is used for calibration of the calorimeter.

Scanning calorimetry

Scanning calorimetric measurements of heat capacity were performed with Setaram DSC-111 and Netzsch-404 DSC calorimeters. The Setaram DSC-111 (a true Calvet microcalorimeter used in scanning mode) operates in the temperature range 300–970 K. Corundum (powdered, 99.997% metals basis) was used as the heat capacity standard. Quartz and hematite were used to judge the accuracy of the data; the data collected for quartz and hematite deviated less than 2% from the C_p of Robie and Hemingway (1995). Heat capacity at high temperatures (300–1550 K) was measured with a high-temperature Netzsch-404 differential scanning calorimeter (DSC). Low-temperature heat capacity was measured with a low-temperature Netzsch-404 DSC in the temperature range 200–400 K. Cooling was provided by liquid nitrogen boil-off. The measurements were performed in an atmosphere of flowing He (40 ml min^{-1}, low-temperature DSC) or air (40 ml min^{-1}, high-temperature DSC). A sapphire disk served as the heat-capacity standard for the Netzsch-404 DSC instruments. Heat capacity was calculated using the software supplied by the manufacturer. The combination of Setaram DSC-111 and Netzsch-404 calorimeters was chosen because the Setaram DSC-111 offers better reproducibility of the data (using ~200 mg of sample) while the Netzsch-404 DSC requires a significantly smaller amount of sample (≤ 50 mg) and operates up to ~1700 K. The collected data were averaged and fitted to a Haas–Fisher polynomial (Haas and Fisher 1976) in the range 298–1550 K.

Mössbauer spectroscopy

[57]Fe Mössbauer spectra of $FeAlO_3$ were obtained in a transmission geometry at 298 K with a microcomputer-controlled spectrometer, operating in a constant acceleration mode. A 25-milliCurie [57]Co/Rh source was employed; this source is known to result in narrow spectral lines. The absorber was prepared using an acetone-Duco cement slurry of 20 mg of $FeAlO_3$ that was allowed to dry in a 2.5-cm circular area on aluminized mylar. The assembly of shielded absorber holder, shielded detector, and velocity drive were aligned on an optical bench which was mounted on a vibration-isolated optical table. The spectrometer was calibrated by means of standard absorbers of sodium nitroprusside and iron metal.

The Mössbauer spectra were obtained at two velocities: one over a range of -4 mm s^{-1} to 4 mm s^{-1} in order to detect the presence of ferrous iron or magnetic impurities, and the other over a range of -2 mm s^{-1} to 2 mm s^{-1} in order to obtain a high-precision spectrum of the $FeAlO_3$ phase. The spectra were analyzed by nonlinear least-squares fits. The spectra were adequately fitted with symmetric quadrupole doublets and Lorentzian line shapes. The details of the data collection and analyses have been given previously (Clark 1997; Dotson 1998).

Molecular modeling

Selected crystal structures were optimized using the program GULP (Gale 1997). After optimization, the program calculated phonon density of states and thermodynamic properties (Helmholtz free energy, entropy, and heat capacity) for the optimized configuration. The core–shell model (Gale 2001) was used for oxygen ions, whereas the cations were represented only by a core with the full formal charge assigned to it. The Al–O and O–O Buckingham potential, spring constant for oxygen core–shell interaction, and the three-body O–Al–O bending potential were taken from Winkler et al. (1991). These potentials were found to reproduce the experimental C_p of corundum with excellent accuracy (average difference $C_{p,tabulated} - C_{v,calculated} = 0.5$ J mol^{-1} K^{-1}, maximum difference 1.5 J mol^{-1} K^{-1}, between 10 and 330 K). For other cation–oxygen pairs, the agreement between calculated and experimental heat capacity was not satisfactory when the potentials of Winkler et al. (1991) were used. The Born–Mayer potentials for Fe^{3+}–O, Ca^{2+}–O, and Mg^{2+}–O were derived by relaxed fitting (Gale 2001) using GULP. The crystal structures for fitting were taken from Rietveld refinement for hematite from this study and the ICSD database (Berndt 1997) for CaO (NaCl structure type, $a = 4.805$ Å) and MgO (NaCl structure type, $a = 4.212$ Å). The entropy and heat capacity values were taken from Robie and Hemingway (1995). The elastic constants for hematite were taken from Liebermann and Maasch (1986), and the elastic constants of periclase and lime were the same as used by Bush et al. (1994). The derived potentials were required to reproduce the experimental crystal structure, heat capacity, and entropy, thus dictating the choice of the weighting scheme for the fitting. The most heavily weighted input parameters were fractional positions of the atoms in the asymmetric cell. An equal and lesser weight was put on lattice parameters and the entropy and heat capacity values. The least weight was attached to the elastic constants. The transferability of the derived potentials (Table 1) to other phases was probed by calculation of vibrational entropy for a number of Ca(Mg)–Fe(Al) phases (Fig. 1). $MgFe_2O_4$ was modeled as a fully ordered inverse spinel. The two quantities in Fig. 1, C_v and C_p, are not strictly comparable, but the difference between the two [as $100 \times (C_p - C_v)/C_p$, where $C_p - C_v = \alpha^2 TV/\beta$] is small, for example 0.8% for corundum and 1.1% for hematite, lime, and periclase at 298 K. While structural parameters test the first derivative of the derived potentials, elastic constants provide a constraint on the second derivative of the potentials. Although the least weight in the fitting procedure was attached to the elastic constants, they were reproduced well by the derived potentials (Table 2), in general better than by the potentials of Bush et al. (1994).

The $FeTiO_3$-like and $LiNbO_3$-like structures of composition $FeAlO_3$ were optimized in full $R\bar{3}$ symmetry. $FeAlO_3$ (with $FeGaO_3$ structure) was optimized by GULP using full symmetry ($Pna2_1$). The atomic positions and lattice parameters were taken from Bouree et al. (1996), but the structure was optimized as fully ordered. One of the Al positions was simulated as tetrahedral and one as octahedral, in agreement with the structural data, the difference between the two being only in equilibrium angle Θ in the three-body bending potential (Table 1). For the optimization of the disordered $FeAlO_3$ with corundum structure, a $2 \times 2 \times 2$ supercell of hematite and corundum was relaxed to P1 symmetry. After convergence with respect to the number of sampled k points was

Table 1 Parameters of the interatomic potentials used for optimization and thermodynamic properties calculation of Ca–Mg–Fe–Al solids. The functional form of the potentials that use the adjustable parameters A, ρ, k, and Θ were given by Winkler et al. (1991)

Atom pair	A	ρ
Fe^{3+}–O	630.096	0.3748
Al^{3+}–O	1460.300	0.29912
Mg^{2+}–O	837.611	0.3233
Ca^{2+}–O	1150.227	0.3406
		k
$O^{0.86902}$ core–$O^{-2.86902}$ shell		60.00
	k	Θ
O–Al^{3+}–O	2.09724	90, 109.47
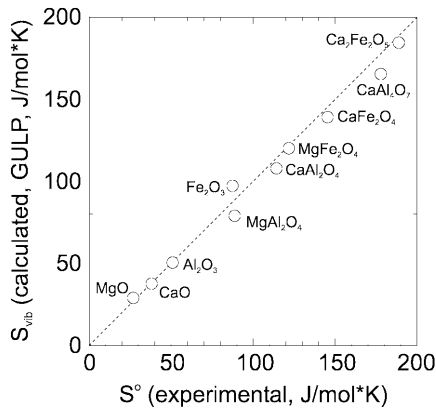
Fig. 1 Comparison of experimental standard entropies and calculated vibrational entropies (GULP, Gale 1997) at 298 K for a number of Ca–Mg–Fe–Al phases. Note that the relationship between the calculated and experimental entropy should not be 1:1 because the experimental entropy includes dilatational entropy and, in the case of Fe-bearing phases, magnetic entropy. Because the magnitude of these contributions is not exactly known, the total standard entropy (from Robie and Hemingway 1995, and from King 1955 for calcium aluminates) is plotted versus the calculated vibrational entropy. The *error bars* on the experimental entropy data are smaller than the symbols

Table 2 Comparison of experimental (Liebermann and Maasch 1986, Bush et al. 1994) and calculated elastic constants (10^{11} dyn cm^{-2}), using the potential parameters in Table 1 and GULP (Gale 1997)

		Corundum	Hematite	Periclase	Lime
c_{11}	exp.	49.69	35.59	29.70	22.35
	calc.	66.52	32.88	29.84	21.73
c_{12}	exp.	16.36	18.50	9.50	9.87
	calc.	29.03	21.89	16.58	9.85
c_{13}	exp.		20.94		
	calc.		7.17		
c_{14}	exp.		−1.04		
	calc.		2.87		
c_{22}	exp.	49.69			
	calc.	66.52			
c_{33}	exp.	49.80	29.92		
	calc.	52.42	28.27		
c_{44}	exp.	14.74	5.80	15.60	9.87
	calc.	14.79	3.66	16.58	9.85

achieved, the results for both phases were found to be identical (within < 0.1%) for optimization using full ($R\bar{3}c$) and relaxed ($P1$) symmetry. The $2 \times 2 \times 2$ supercell contains 96 metal cations. Ninety-two random and distinct configurations of the $2 \times 2 \times 2$ supercell with 48 iron and 48 aluminum atoms were generated (symmetry $P1$) and optimized by GULP.

Results

Hematite–corundum solid solution

The enthalpies of drop solution for the high-T hematite–corundum samples, determined in lead borate solvent at 1075 K, are listed in Table 3. The enthalpies of formation from oxides ($\Delta H_{f,\text{oxides}}$) (Table 3) were calculated using a thermochemical cycle outlined in Table 4. The $\Delta H_{f,\text{oxides}}$ values are equal to the enthalpies of mixing (ΔH_{mix}). The hematite–corundum samples show positive deviation from ideal mixing (Fig. 2a).

The low-T Al-hematite samples, prepared by decomposition of Al-goethite at 975 K, can be expected to be different from the Al-hematite synthesized at 1623 K, in terms of their particle size and excess water content. The calorimetric data, determined in lead borate at 975 K, are given in Table 5. The excess water (Table 5) was treated as bulk liquid water in the thermochemical cycle (Table 6). The enthalpies of mixing for these Al-hematite samples are positive, at both 298 and 975 K (Table 5; Fig. 2a,b). Furthermore, the ΔH_{mix} values at 298 K and 975 K overlap within their respective uncertainties (Table 5). Thus, ΔH_{mix} is independent of temperature.

The lattice parameters of Al-hematite show deviation from ideal behavior (Vegard's law) (Fig. 3), in agreement with Barron et al. (1984) and Schwertmann et al. (1979). The magnitude of the deviation from Vegard's law is not only a function of Al substitution in hematite but also depends on the history of the sample. The volume of mixing and lattice parameter a for the high-T Al-hematite samples show smaller deviation than those for the low-T Al-hematite. While the lattice parameter c of the low-T Al-hematite shows positive deviation from Vegard's law, high-T Al-hematite shows a slight negative deviation. The lattice parameter c of Fe-corundum shows slight negative deviation, and the lattice parameter a even smaller positive deviation. These virtually compensate each other to approximate an ideal (zero) volume of mixing. These crystallographic differences between low- and high-temperature samples do not seem to affect their energetics significantly, as discussed above.

FeAlO3

The enthalpy of formation of $FeAlO_3$ (with $FeGaO_3$ structure) from hematite and corundum (27.9 ± 1.8 kJ mol^{-1}, Table 3) was determined for the first time in this study. The enthalpy of formation from

Table 3 Chemical composition (q), lattice parameters (a,c), fractional atomic positions (x,0,1/4 for oxygen; 0,0,z for metal) and statistics of the Rietveld refinement (χ^2, wR_p) (for hematite-rich samples only), and the enthalpy changes measured and calculated for the high-T hematite–corundum samples and FeAlO$_3$. The *subscripts on enthalpies* refer to reaction numbers in Table 4

Sample	q mol mol^{-1} as [Fe/(Fe + Al)]	x for oxygen z for Fe/Al	χ^2 wR_p	a (Å) c (Å)	$\Delta H_{1,2,3}$ (kJ mol^{-1})	$\Delta H_{f,\text{oxides}} = \Delta H_4$ (kJ mol^{-1})
Hematite	1	0.3553(1)[d] 0.3119(9)	2.13 0.2049	5.0367(1)[d] 13.7550(4)	189.91[a] ± 0.94[b](27)[c]	0
AL-1.6	0.966[a] ± 0.001[b](24)[c]	0.3554(1) 0.3117(9)	1.74 0.1773	5.0283(2) 13.7275(9)	182.29 ± 1.54(14)	5.3 ± 1.8
AL-1.8	0.908 ± 0.001(27)	0.3550(1) 0.313(1)	1.97 0.1864	5.0140(3) 13.6783(12)	171.72 ± 1.71(15)	11.8 ± 1.9
AL-1.9	0.878 ± 0.002(14)	0.3553(1) 0.310(1)	1.77 0.1744	5.0081(2) 13.6579(9)	173.93 ± 1.12(9)	7.5 ± 1.4
AL-1.12	0.502 ± 0.001(12)			$a = 4.9842(2)$ $b = 8.5544(4)$[e] $c = 9.2347(5)$	127.36 ± 1.74(17)	27.9 ± 1.8
AL-1.16	0.091 ± 0.002(14)			4.7874(1) 13.0545(3)	115.88 ± 1.63(14)	10.8 ± 1.7
AL-1.17	0.061 ± 0.002(9)			4.7783(1) 13.0350(2)	118.63 ± 1.22(11)	6.0 ± 1.3
AL-1.18	0.029 ± 0.001(13)			4.7693(2) 13.0159(6)	118.30 ± 1.41(20)	4.1 ± 1.5
Corundum	0			4.7618(6) 12.9981(18)	120.38 ± 0.54(41)	0

[a] Average
[b] Two standard deviations of the mean
[c] Number of experiments
[d] Atomic position or lattice parameter and estimated standard deviation on the last decimal digit
[e] The structure of the FeAlO3 phase has an orthorhombic symmetry

Table 4 Thermochemical cycle for the high-T Al-hematite and Fe-corundum samples and FeAlO$_3$

Reaction and reaction number	
α-Fe$_2$O$_3$ (cr, 298) = α-Fe$_2$O$_3$ (sol, 1075)[a]	1
α-Al$_2$O$_3$ (cr, 298) = α-Al$_2$O$_3$ (sol, 1075)	2
(Fe$_q$Al$_{1-q}$)$_2$O$_3$ (cr, 298) = q α-Fe$_2$O$_3$ (sol, 1075) + $(1-q)$ α-Al$_2$O$_3$ (sol, 1075)	3
q α-Fe$_2$O$_3$ (cr, 298) + $(1-q)$ α-Al$_2$O$_3$ (cr, 298) = (Fe$_q$Al$_{1-q}$)$_2$O$_3$ (cr, 298)	4
$\Delta H_1 = \Delta H_{\text{dsol}}(\alpha\text{-Fe}_2\text{O}_3)$[b]	
$\Delta H_2 = \Delta H_{\text{dsol}}(\alpha\text{-Al}_2\text{O}_3)$[b]	
$\Delta H_3 = \Delta H_{\text{dsol}}[(\text{Fe}_q\text{Al}_{1-q})_2\text{O}_3]$[b]	
$\Delta H_4 = \Delta H^o_{f,\text{oxides}} = q\ \Delta H_1 + (1-q)\ \Delta H_2 - \Delta H_3$[b]	

[a] cr = crystalline solid; sol = solution in lead borate
[b] This study; data in Table 3

oxides of a hypothetical disordered FeAlO$_3$ phase with corundum structure is 29.0 ± 2.5 kJ mol^{-1}, calculated from $\Delta H_{f,\text{oxides}} = \Delta H_{\text{mix}} = (116 \pm 10)X_{\text{cor}}(1 - X_{\text{cor}})$ at $X_{\text{cor}} = 0.5$. The oxidation state of Fe in FeAlO$_3$ was explored by Mössbauer spectroscopy because any presence of ferrous iron could significantly alter the calorimetric results. Within the limits of the sensitivity of Mössbauer spectroscopy ($\sim$0.1 wt% Fe^{2+}), no ferrous iron was detected in the FeAlO$_3$ sample. Neither were any magnetically ordered impurity phases (hematite, magnetite–hercynite) detected.

The standard entropy of FeAlO$_3$ has not been measured previously. The vibrational contribution to S^o can be estimated by integrating over the calculated phonon density of states (using GULP). The phonon calculations were tested for convergence with respect to the number of sampled k points. The vibrational entropy of FeAlO$_3$ at 298 K was calculated as $S_{\text{vib}} = 75.2$ J mol^{-1} K^{-1}, larger than the mean of experimentally determined vibrational and dilatational entropies of hematite and corundum of 67.9 J mol^{-1} K^{-1}.

Bouree et al. (1996) investigated the crystal and magnetic structure of FeAlO$_3$ by neutron diffraction. They found that the phase is ferrimagnetic at 30 K and paramagnetic at 298 K. They also stated that FeAlO$_3$ undergoes a magnetic transition at $\sim$280 K, but provided neither experimental evidence nor a literature reference supporting this datum. Our heat capacity measurements show no detectable C_p anomaly between 240 and 1550 K. The phase is paramagnetic at 298 K, as indicated by the presence of a single doublet in the Mössbauer spectrum (Fig. 4) and small positive magnetic susceptibility. In this case, the magnetic contribution to entropy at 298 K (i.e., well above the magnetic transition temperature) is $S_{\text{mag}} = nR\ln(2S+1)$ (Gopal 1966), where S is the spin of the magnetic ions (in this

520

case 5/2), and n is the number of magnetic ions in the formula. For FeAlO$_3$, S_{mag} = 14.9 J mol^{-1} K^{-1}.

Bouree et al. (1996) refined atomic positions and occupancies of Fe and Al at four distinct crystallographic sites in the structure of FeAlO$_3$. We have attempted to refine all these parameters by a Rietveld refinement of the powder XRD pattern. The refinement
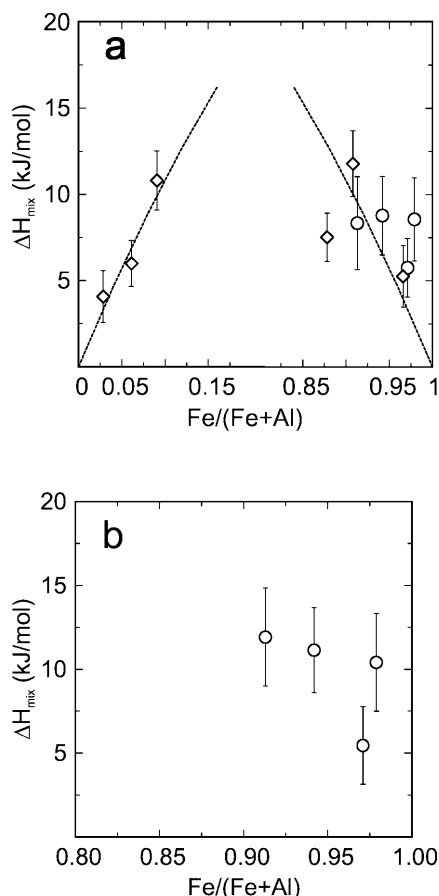

of occupancies from the XRD powder pattern gave an incorrect composition, Fe$_{0.72}$Al$_{1.28}$O$_3$. Fazey et al. (1991), in their Rietveld refinement of Al-goethite, were also unable to refine the Fe/Al occupancy of the metal sites. The reason for this inability to refine the correct occupancies from powder XRD data remains unclear. Our results are at least in qualitative agreement with the results of Bouree et al. (1996), showing that the tetrahedral site has a strong preference for Al [Fe/(Fe + Al) = 0.09(2) (this work), Fe/(Fe + Al) = 0.10(1) (Bouree et al. 1996)], and the regular octahedral site also prefers Al [0.27(2), 0.34(1)]. Bouree et al. (1996) determined that the two irregular sixfold sites are occupied mostly by iron [site 1: 0.49(4), 0.78(1), site 2: 0.58(2), 0.76(1)]. The configurational entropy is $S_{conf} = -R\Sigma$ [$X_i$lnX$_i$ + (1 − X_i)ln(1 − X_i)], where X_i is the mole fraction of Fe on the i-th site. Using the data of Bouree et al. (1996), S_{conf} = 8.5 J mol^{-1} K^{-1} (mol^{-1} FeAlO$_3$).

The Mössbauer spectrum provides additional evidence of a disordered distribution of Fe over several sites, consistent with the XRD refinement data. The spectrum is asymmetric, with one line being broader and less intense than the other, and with appreciable variations in the electric quadrupole splittings but a narrower range of isomer shifts (Table 7). The isomer shift is characteristic of ferric iron in octahedral sites in insulating oxides. The explanation of the variation in electric quadrupole splitting is more ambiguous; however, for the ferric ion, it is not unreasonable to associate the larger quadrupole splitting with the more distorted site. The difference in the linewidths is noteworthy. The smaller value is typical of ferrites with the ferric ion on a single site. The larger value is a strong indication of substantial local disorder, e.g. variations in the site parameters and/or environment of neighboring ions. The iron sites giving rise to the two subspectra occur with roughly equal frequencies.

Dilatational entropy [$S_{dil} = \int^T (C_p − C_v)dlnT$] represents the smallest contribution to the standard entropy. The S_{dil} for corundum is 0.20 J mol^{-1} K^{-1}, for hematite 0.38 J mol^{-1} K^{-1}. We assume that the S_{dil} of FeAlO$_3$ is close to the mean of the S_{dil} for hematite and corundum, 0.3 J mol^{-1} K^{-1}, and use this value for S_{dil}(FeAlO$_3$).

The standard entropy of FeAlO$_3$ is then the sum of vibrational, magnetic, and dilatational entropy; addition

Fig. 2 a Enthalpies of mixing in the hematite–corundum solid solution at 298 K (low-T Al-hematite *circles*; high-T hematite–corundum *diamonds*) (per two cations). The *dashed curve* is the best fit [116 ± 10 X_{hem}(1−X_{hem})] for the ΔH_{mix} for the high-T samples. **b** Enthalpies of mixing in the hematite–corundum solid solution at 975 K

Table 5 Excess water content (v), and the enthalpy changes measured and calculated for the low-T Al-hematite samples. The *subscripts on enthalpies* refer to reaction numbers in Table 6

Sample	v (mol of H$_2$O)	ΔH_5 (kJ mol^{-1})	ΔH_6 (kJ mol^{-1})	ΔH_{mix}(298 K) = ΔH_{13} (kJ mol^{-1})	ΔH_{mix}(975 K) = ΔH_{10} (kJ mol^{-1})
hem-AL0	0.020[a] ± 0.005[b](8)[c]	168.12[a] ± 1.97[b](8)[c]	95.83[a] ± 1.58[b](8)[c]	–	–
hem-AL3	0.012 ± 0.005(7)	161.60 ± 2.05(8)	99.11 ± 1.61(11)	8.56 ± 2.41	10.41 ± 2.92
hem-AL6	0.016 ± 0.005(6)	164.08 ± 1.14(9)	96.98 ± 1.52(8)	5.76 ± 1.69	5.45 ± 2.31
hem-AL14	0.029 ± 0.009(6)	160.22 ± 1.95(8)	99.95 ± 1.03(9)	8.78 ± 2.29	11.14 ± 2.54
hem-AL20	0.025 ± 0.005(6)	158.55 ± 2.43(8)	100.24 ± 1.07(9)	8.34 ± 2.70	11.92 ± 2.92

[a] Average
[b] Two standard deviations of the mean
[c] Number of experiments

Table 6 Thermochemical cycle for low-T Al-hematite samples

Reaction and reaction number	
$(Fe_qAl_{1-q})_2O_3(cr,298) + vH_2O(l,298) = qFe_2O_3(sol,975) + (1-q)Al_2O_3(sol,975) + vH_2O(g,975)^a$	5
$(Fe_qAl_{1-q})_2O_3(cr,298) + vH_2O(l,298) = (Fe_qAl_{1-q})_2O_3(cr,975) + vH_2O(g,975)$	6
$H_2O(l,298) = H_2O(g,975)$	7
$\alpha\text{-}Fe_2O_3 (cr,975) = Fe_2O_3(sol,975)$	8
$\alpha\text{-}Al_2O_3 (cr,975) = Al_2O_3(sol,975)$	9
$q\,\alpha\text{-}Fe_2O_3 (cr,975) + (1-q)\alpha\text{-}Al_2O_3 (cr,975) = (Fe_qAl_{1-q})_2O_3(cr,975)$	10
$\alpha\text{-}Fe_2O_3 (cr,298) = Fe_2O_3(sol,975)$	11
$\alpha\text{-}Al_2O_3 (cr,298) = Al_2O_3(sol,975)$	12
$q\,\alpha\text{-}Fe_2O_3 (cr,298) + (1-q)\,\alpha\text{-}Al_2O_3 (cr,298) = (Fe_qAl_{1-q})_2O_3(cr,298)$	13

$\Delta H_5 = \Delta H_{dsol} [(Fe_qAl_{1-q})_2O_3]^b$
$\Delta H_6 = \Delta H_{ttd} [(Fe_qAl_{1-q})_2O_3]^b$
$\Delta H_7 = H_{975}\text{-}H_{298} (H_2O) = 69.0^c \text{ kJ mol}^{-1}$
$\Delta H_8 = \Delta H_{sol} (\alpha\text{-}Fe_2O_3) = \Delta H_{11} - (96.86 \pm 0.42^d) = 73.73 \pm 1.35 \text{ kJ mol}^{-1}$
$\Delta H_9 = \Delta H_{sol} (\alpha\text{-}Al_2O_3) = \Delta H_{12} - [H_{975}\text{-}H_{298} (\alpha\text{-}Al_2O_3)^c] = 33.56 \pm 0.60 \text{ kJ mol}^{-1}$
$\Delta H_{10} = \Delta H_{mix} (975 \text{ K}) = -\Delta H_5 + \Delta H_6 + q\Delta H_8 + (1-q) \Delta H_9{}^b$
$\Delta H_{11} = \Delta H_{dsol} (\alpha\text{-}Fe_2O_3) = 170.59 \pm 1.29^d \text{ kJ mol}^{-1}$
$\Delta H_{12} = \Delta H_{dsol} (\alpha\text{-}Al_2O_3) = 108.46 \pm 0.60^e \text{ kJ mol}^{-1}$
$\Delta H_{13} = \Delta H_{mix} (298 \text{ K}) = -\Delta H_6 + v\Delta H_7 + q\Delta H_{11} + (1-q) \Delta H_{12}{}^b$

[a] cr = crystalline solid; l = liquid; g = gas; sol = solution in lead borate
[b] This study; data in Table 5
[c] Calculated from Robie and Hemingway (1995)
[d] This study
[e] Majzlan et al. (2000)

of the configurational entropy gives $S^o_{298} = 98.9$ J mol^{-1} K^{-1}. The Gibbs free energy formation of $FeAlO_3$ from oxides at 298 K is $+19.1 \pm 1.8$ kJ mol^{-1}; therefore, $FeAlO_3$ is not stable at 298 K with respect to hematite and corundum. The Gibbs free energy of formation of $FeAlO_3$ from elements is -1144.2 ± 2.0 kJ mol^{-1}.

The measured heat capacity of $FeAlO_3$ in the temperature range 298–1550 K was fitted by a Haas–Fisher polynomial $C_p(T) = 175.8 - 0.002472T - (1.958 \times 10^6)/T^2 - 917.3/T^{0.5} + (7.546 \times 10^{-6})T^2$. For the thermodynamic calculations (below), the same polynomial was used up to 1700 K because the slope of the C_p curve remains small and constant up to at least 1700 K.

Discussion

Thermodynamics of hematite–corundum solid solution

The enthalpies of mixing in the hematite–corundum solid solution can be used to calculate the position of the solvus between these two end members, and compare the calculated solvus to the experimentally determined solvus of Muan and Gee (1956). The enthalpies of mixing (Table 3) can be fitted by a polynomial $WX_{hem}(1-X_{hem})$, where W is the temperature-independent interaction parameter with value of 116 ± 10 kJ mol^{-1} and X_{hem} is the mole fraction of hematite in the solid solution. All values of interaction parameters are reported here per two cations in $(Fe,Al)_2O_3$; the uncertainties are two standard deviations of the mean. Therefore, as a first approximation, regular solution behavior can be assumed. Doing so, we find that the thermochemical data from this study overestimate the extrapolated position of the crest of the solvus. The exact position of the crest of the solvus is not known because the stability field of Al-hematite is intersected by the stability field of $FeAlO_3$ above 1591 K and Fe–Al spinel at temperatures $> \sim 1800$ K (Muan and Gee 1956). However, an interaction parameter $W = 69 \pm 5$ kJ mol^{-1}, calculated from the phase diagram of Muan and Gee (1956), documents the difference between the regular solution model based on our data and the phase diagram. The slight asymmetry of the solvus can be accounted for in the subregular solution model where $\Delta G_{excess} = X_{hem}X_{cor} (W_{G,cor}X_{hem} + W_{G,hem}X_{cor})$. Fitting the solvus of Muan and Gee (1956) gives $W_{G,cor} = 62 \pm 4$ and $W_{G,hem} = 74 \pm 4$ kJ mol^{-1}. Similar values of these two interaction parameters suggest that the asymmetry, if it exists, is quite small (note that if $W_{G,hem} = W_{G,cor}$ then the solvus is symmetric). Hence, we feel that neither the experimental points of Muan and Gee (1956) nor our data are a strong indication of an asymmetric solvus. The ΔH_{mix} values do not change significantly with temperature (Table 5), and excess entropies must be included in the thermodynamic description of the hematite–corundum solid solution in order to reproduce the phase diagram. Using our mixing enthalpies, the hematite–corundum solvus can be approximately reproduced by a symmetric, regular-like solution model with a temperature-dependent interaction parameter $W = W_H - TW_S$, where $W_H = 116 \pm 10$ kJ mol^{-1} and $W_S = 32 \pm 4$ J mol^{-1} K^{-1}. Irrespective of the solution model adopted, the equilibrium solubility of hematite in corundum and vice versa at
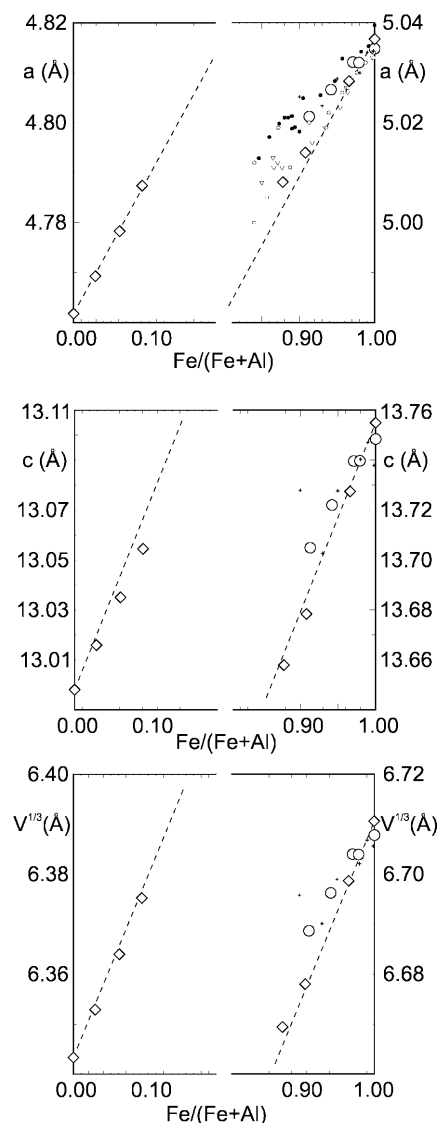
Fig. 3 Lattice parameters and volume of the unit cell in the hematite–corundum solid solution as a function of Al(Fe) substitution in hematite(corundum). *Large symbols*: high-T hematite–corundum (*diamonds*); low-T Al-hematite (*circles*). *Small symbols*: Schwertmann et al. (1979), Barron et al. (1984), Wells et al. (2001), Van San et al. (2001). The *dashed lines* represent Vegard's rule (ideal mixing)

298 K is essentially zero, and Al-hematite found in natural low-temperature environments in metastable with respect to hematite and corundum.

Thermodynamics of FeAlO₃

The thermodynamic stability of $FeAlO_3$ (with $FeGaO_3$ structure) was explored here for the first time. The contradictory experimental evidence is not helpful in evaluation of thermodynamic stability of the ternary phase $FeAlO_3$. Muan and Gee (1956) could neither synthesize nor decompose the phase below 1591 K. They also determined its upper temperature stability limit to 1673 K, when $FeAlO_3$ transforms to Fe–Al spinel and
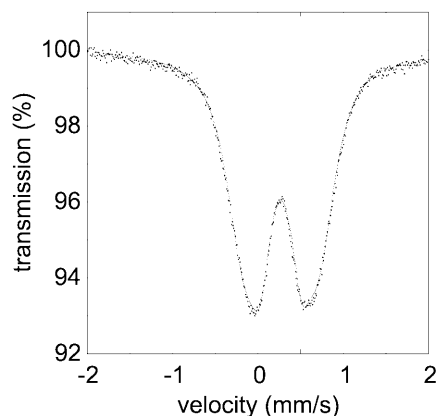

Fig. 4 Mössbauer spectrum of $FeAlO_3$

Table 7 ^{57}Fe Mössbauer spectroscopic parameters of $FeAlO_3$ at 298 K. All isomer shifts are relative to iron metal

	Quadrupole splitting (mm s^{-1})	Isomer shift (mm s^{-1})	Linewidth (FWHM) (mm s^{-1})	Relative intensity
Subspectrum 1	0.505(6)	0.336(6)	0.349(6)	45%
Subspectrum 2	0.933(6)	0.342(6)	0.453(10)	55%

Fe–corundum. Polli et al. (1996) prepared $FeAlO_3$ at ~1073 K by heating nanocrystalline γ-$(Fe,Al)_2O_3$. Prolonged heating (24 h at 1073 K) resulted in partial transformation of $FeAlO_3$ into Al-hematite and Fe-corundum. MacKenzie and Berezowski (1984) observed (by XRD and Mössbauer spectroscopy) $FeAlO_3$ in a mixture of phases prepared by thermal decomposition of aluminous berthierine at temperatures 1223–1473 K. Donnet (1993) prepared a mixture of Fe–Al oxides with $FeAlO_3$ by annealing an Fe-ion-implanted corundum disk at temperatures between 1273 and 1673 K. We were able to synthesize the phase by annealing the nitrate precursors as well as a corundum and hematite mixture at 1623 K.

The enthalpic contribution to the free energy of Fe-AlO_3 destabilizes the phase with respect to hematite and corundum from 298 up to 1700 K. Because the phase can be synthesized from its constituent oxides, it must be entropy-stabilized at high temperatures. At room temperature, the sum of S_{vib}, S_{conf} and S_{dil} of $FeAlO_3$ is $75.2 + 8.5 + 0.3 = 84.0$ J mol^{-1} K^{-1}. The difference between this value and the mean of S_{vib} and S_{dil} for hematite and corundum (67.9 J mol^{-1} K^{-1}) is 16.1 J mol^{-1} K^{-1}. Note that above the Néel transition in Fe_2O_3 (950 K), $1/2(Fe_2O_3 + Al_2O_3)$ and $FeAlO_3$ both have the same magnetic entropy, so the magnetic contribution to the entropy of formation is zero. Assuming temperature-independent enthalpy of formation of $FeAlO_3$ from oxides, the entropy needed to compensate the unfavorable enthalpy at the lower stability limit of $FeAlO_3$ (1591 K) is (27.9 ± 1.8 kJ mol^{-1})/1591 K = 17.5 ± 1.1 J mol^{-1} K^{-1}. Hence, the entropy needed to stabilize the phase approximately matches the entropy difference between $FeAlO_3$ and hematite and corundum.

Molecular modeling

Helmholtz free energy (ΔF) was calculated for each optimized $FeAlO_3$ structure in order to explore the energetics of ordered and disordered $FeAlO_3$ phases. The calculated data for $FeGaO_3$- and corundum-like $FeAlO_3$ can be compared to the experimental results of this study. For the reactions where both reactants and products are solids, $\Delta F = \Delta H + P\Delta V \approx \Delta H$, and therefore the $\Delta F_{calculated}$ and $\Delta H_{experimental}$ can be compared (Fig. 5). For example, for the reaction between hematite, corundum, and $FeAlO_3$, the $P\Delta V$ term at $P = 1$ bar accounts for 0.2 J, as opposed to the ΔH term of 27 900 J. The ordered ilmenite- and $LiNbO_3$-like $FeAlO_3$ phases were never reported to be synthesized or found in nature. Consequently, their energetics can be explored only through the calculations, bearing the limitations of such calculations in mind. All optimized $FeAlO_3$ structures are higher in energy than a mechanical mixture of hematite and corundum. In agreement with the experiment, the $FeGaO_3$-like structure is stable with respect to the corundum-like disordered $FeAlO_3$. The $FeTiO_3$- and $LiNbO_3$-like configurations are stable with respect to disordered corundum-like $FeAlO_3$, suggesting that there may be a driving force favoring ordering in the hematite–corundum solid solution. At high temperatures, when entropy plays an increasingly important role, the $FeGaO_3$-like structure is favored over the fully ordered ($FeTiO_3$- and $LiNbO_3$-like) phases by its entropy.

Fitting a regular-like solution model to our data gives an estimate of the enthalpy of mixing for fully disordered $(Fe,Al)_2O_3$, neglecting possible short-range cation
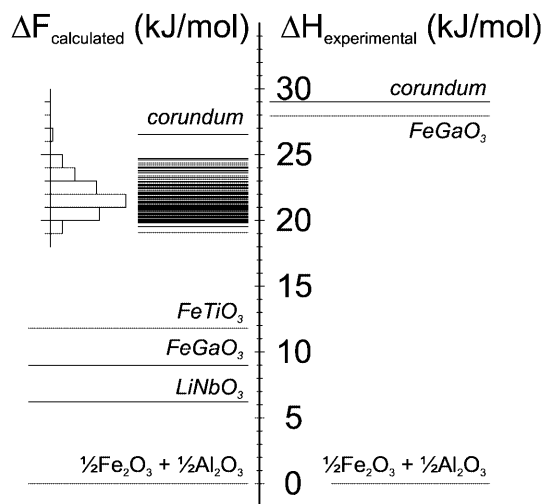

Fig. 5 A comparison of $\Delta H_{experimental}$ for the $FeGaO_3$- and corundum-like $FeAlO_3$ structures, and $\Delta F_{calculated}$ (GULP, Gale 1997) for $FeTiO_3$-, $LiNbO_3$-, $FeGaO_3$- and corundum-like $FeAlO_3$ structures. The mechanical mixture of hematite and corundum ($1/2Fe_2O_3 + 1/2Al_2O_3$) corresponds to the zero of energy. The structure type of each $FeAlO_3$ phase is indicated *in italics*. The results of energy calculations for all 92 corundum-like $FeAlO_3$ structures are shown, together with a histogram of distribution of the calculated energies

order. Any possible short-range order could be potentially investigated by annealing samples of intermediate composition at variable time and temperature, just like for the hematite–ilmenite solid solution (Brown and Navrotsky 1994). In the hematite–corundum series, the intermediate compositions cannot be synthesized, because at these compositions, clustering of Fe and Al and unmixing of hematite and corundum occurs. Hence, possible short-range order can be explored only through computations. Becker et al. (2000) presented a theoretical study on barite-celestine ($BaSO_4$–$SrSO_4$) solid solution, including the role of short-range order in this solid solution. They have shown that at low temperatures (< 800 K), the short-range order leads to a reduction in the enthalpies of mixing, with several ordered configurations located in local energy minima. We have attempted to perform similar Monte Carlo calculations on the hematite–corundum solid solution. However, because all simulated configurations had composition $Fe_{48}Al_{48}O_{96}$, the matrix necessary to derive the interaction energies (see Eq. 1 of Becker et al. 2000) was too close to numerically singular, and these calculations were abandoned. Even if we proceeded with the computational experiment, it would be restricted to corundum-like structures, never reaching the $FeGaO_3$-like configuration which actually shows up as an intermediate phase.

For the solid-solution compositions accessible experimentally, the regular-like solution model is a satisfactory description. These compositions are dilute, and little or no short-range ordering can be expected. The postulated temperature-independent enthalpies of mixing are also valid for the dilute compositions. The existence of intermediate composition with corundum-like structure was never reported, ordered or not. Two factors are responsible for the absence of the intermediate compositions. The first one is of thermodynamic nature, and lies in the stability of the $FeGaO_3$-like phase at intermediate temperatures. The second factor is kinetic: the system reacts sluggishly even at 1500 K (Muan and Gee 1956), and at low temperatures, when the driving force for ordering might increase, the slow diffusion of ions through the structure prohibits the structure to achieve any lower-energy, ordered state.

Crystallography of hematite–corundum solid solution

Changes in the structure of Al-hematite were investigated by Schwertmann et al. (1979), who found that the full width at half maximum of all diffraction peaks of Al-hematite had a minimum between 3 and 5 mol% substitution. They attributed this observation to "lattice strain relief through small amounts of the smaller Al cation in the octahedral positions". In their Mössbauer spectroscopy study of Al-hematite, De Grave et al. (1988) detected a sharp maximum in Debye temperature and isomer shift at composition $Fe_{0.96}Al_{0.04}O_3$. There is no indication of such behavior in our thermochemical

data, but the energy associated with strain in minerals (e.g., Liu et al. 1995) may be too small to be detected. On the other hand, the X-ray diffraction data collected in this study support the observations of Schwertmann et al. (1979) and De Grave et al. (1988). The crystal structure of hematite or corundum is completely described by four parameters: lattice parameters a and c and the parameters in fractional atomic position of the metal $(0, 0, z)$ and oxygen $(x, 0, 1/4)$. The value of z remains the same over the Al substitution range achieved in this study (Tables 3, 8; Fig. 6a). The x value shows greater variability (Tables 3, 8; Fig. 6b), although the small scattering power of oxygen, as compared to that of iron, leads to significantly larger uncertainties in the positional parameters of oxygen. The variation of the parameter x can be approximated by a quadratic function with a maximum at $\sim Fe_{0.95}Al_{0.05}O_3$. To visualize the structural changes, note that the oxygen ions reside in an arrangement close to hexagonal close-packing in layers stacked along the z axis. Regular hexagonal close-packing would be achieved for oxygen position $(1/3, 0, 1/4)$ (Fig. 6b). Decreasing value of x causes progressive distortion of the hexagonal network (Fig. 6b). Thus, a small amount of aluminum substitution allows the hexagonal network of oxygen ions to adopt a more regular arrangement but further Al substitution enhances the distortion of the hexagonal network. The character of changes in the Al-hematite structure can be further investigated through calculation of the displacement of the cation from the centroid of the octahedron and the sphericity of the octahedron, as defined by Balić-Žunić and Makovicky (1996). The sphericity of the octahedron, related to the standard deviation of the distance between the centroid and the ligands, remains unchanged with increasing Al substitution. The displacement of the cation, on the other hand, varies. It is interesting to notice that the displacement is different for the high-T and low-T Al-hematite samples, most likely manifesting the different degree of OH^- for O^{2-} substitution in the structure. The

data for both series can be approximated with a quadratic polynomial with a maximum at $\sim Fe_{0.96}Al_{0.04}O_3$ (Fig. 7). Thus, the changes observed by Schwertmann et al. (1979) and De Grave et al. (1988) are caused by a variable degree of distortion of the hexagonal network of oxygen ions.
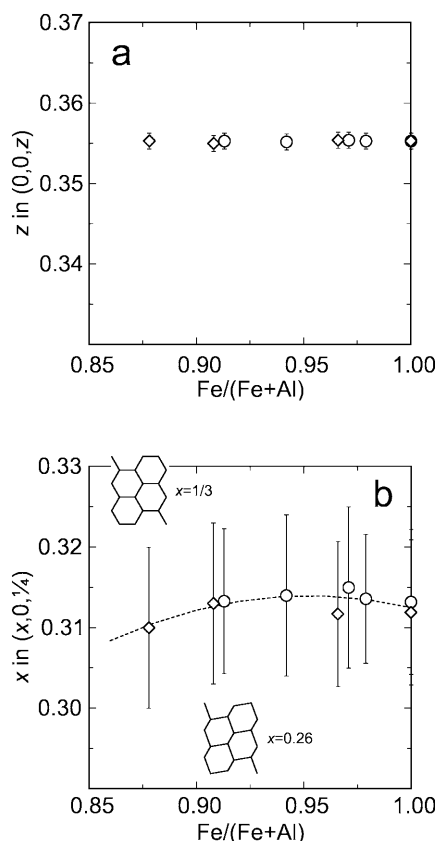

Fig. 6a, b Atomic positions in the hematite-corundum solid solution (low-T Al-hematite *circles*; high-T Al-hematite *diamonds*) **a** Metals (Fe/Al). **b** Oxygen. The degree of distortion of the oxygen network is shown schematically in **b** for oxygen atoms in positions $(1/3, 0, 1/4)$ or $(0.26, 0, 1/4)$

Table 8 Chemical composition (q), lattice parameters (a,c), fractional atomic positions ($x,0,1/4$ for oxygen; $0,0,z$ for metal) and statistics of the Rietveld refinement (χ^2, wR_p) for the low-T Al-hematite samples. Estimated standard deviation on the last decimal place on the lattice parameters or atomic positions given *in parentheses*

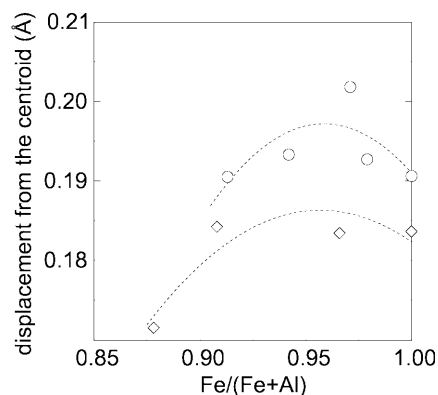| Sample	q [mol mol^{-1}] of Fe/(Al + Fe)]	a (Å) c (Å)	x for oxygen z for Fe/Al	χ^2 wR_p
hem-AL0	1	5.0348(1) 13.7484(4)	0.3553(1) 0.3132(9)	2.33 0.1886
hem-AL3	0.979	5.0320(1) 13.7397(5)	0.3553(1) 0.3136(8)	2.10 0.1708
hem-AL6	0.971	5.0321(4) 13.7396(13)	0.3554(1) 0.315(1)	2.00 0.2056
hem-AL14	0.942	5.0266(2) 13.7220(7)	0.3552(1) 0.314(1)	2.71 0.2073
hem-AL20	0.913	5.0212(2) 13.7049(7)	0.3553(1) 0.3133(9)	2.34 0.1958

Fig. 7 Displacement of central ion in the hematite-corundum solid solution: low-T Al-hematite (*circles*), high-T hematite–corundum (*diamonds*)

Conclusions

The mixing enthalpies in the hematite–corundum solid solution series are positive. The mixing enthalpies alone are not sufficient to reproduce the experimental phase diagram of Muan and Gee (1956), and excess entropies in the solid solution should be considered. The volume of mixing is positive for Al-hematite but almost ideal for Fe-corundum. Moreover, the degree of deviation from Vegard's law for Al-hematite depends on the history of the samples. Introduction of Al into the hematite structure causes varying distortion of the hexagonal network of oxygen ions while the position of the metal ions remains intact.

The ternary phase $FeAlO_3$ is unstable in enthalpy with respect to hematite and corundum at 298 K. It is entropy-stabilized at high temperatures. $FeAlO_3$ contains no ferrous iron as determined by Mössbauer spectroscopy.

References

Anovitz LM, Perkins D, Essene EJ (1991) Metastability in near-surface rocks of minerals in the system Al_2O_3–SiO_2–H_2O. Clays Clay Miner 39: 225–233

Balić-Žunić T, Makovicky E (1996) Determination of the centroid or "the best centre" of a coordination polyhedron. Acta Crystallogr (B)52: 78–81

Barron V, Rendon JL, Torrent J, Serna CJ (1984) Relation of infrared, crystallochemical, and morphological properties of Al-substituted hematites. Clays Clay Miner 32: 475–479

Becker U, Fernandez-Gonzalez A, Prieto M, Harrison R, Putnis A (2000) Direct calculation of the thermodynamic properties of the barite/celestite solid solution from molecular principles. Phys Chem Miner 27: 291–300

Berndt M (1997) ICSD/RETRIEVE version 2.01. Gmelin Institute, FIZ Karlsruhe

Blake RL, Hessevick RE, Zoltai T, Finger LW (1966) Refinement of the hematite structure. Am Mineral 51: 123–129

Bouree F, Baudour JL, Elbadraoui E, Musso J, Laurent C, Rousset A (1996) Crystal and magnetic structure of piezoelectric, ferrimagnetic and magnetoelectric aluminium iron oxide $FeAlO_3$ from neutron powder diffraction. Acta Crystallogr (B) 52: 217–222

Brown NE, Navrotsky A (1994) Hematite-ilmenite (Fe_2O_3–$FeTiO_3$) solid solutions: the effects of cation ordering on the thermodynamics of mixing. Am Mineral 79: 485–496

Bush TS, Gale JD, Catlow RA, Battle PD (1994) Self-consistent interatomic potentials for the simulation of binary and ternary oxides. J Mater Chem 4: 831–837

Cheng T, Bereman R, De Grave E, Bowen LH (2001) A study of aluminum-substituted iron dextran complexes by Mössbauer spectroscopy and X-ray diffraction. Chem Mater 13: 136–140

Clark TM (1997) Local crystal chemical structures at iron sites in amorphous, magnetic, and nanocrystalline materials. PhD Thesis, University of Michigan

Cornell RM, Schwertmann U (1996) The iron oxides. Wiley VCH, Weinheim, 573 pp

De Grave E, Bowen LH, Amarasiriwardena DD, Vandenberghe RE (1988) ^{57}Fe Mössbauer effect study of highly substituted aluminum hematites: determination of the magnetic hyperfine field distributions. J Magn Magn Mater 72: 129–140

Donnet C (1993) Microstructure and thermochemistry of ion-implanted sintered alumina. Appl Surf Sci 68: 19–33

Dotson CR (1998) Order-disorder phenomena in naturally occurring metal oxides, PhD Thesis, University of Michigan

Fazey PG, O'Connor BH, Hammond LC (1991) X-ray powder diffraction Rietveld characterization of synthetic aluminum-substituted goethite. Clays Clay Miner 39: 248–253

Finger LW, Hazen RM (1978) Crystal structure and compression of ruby to 46 kbar. J Appl Phys 49: 5823–5826

Gale JD (1997) GULP: a computer program for the symmetry-adapted simulation. J Chem Soc, Faraday Trans 93: 629–637

Gale JD (2001) Simulating the crystal structures and properties of ionic materials from interatomic potentials. In: Cygan RT, Kubicki JD (eds) Molecular modeling theory: application in the geosciences. Rev Mineral Geochem 42: 37–62

Gopal ESR (1966) Specific heats at low temperatures. Plenum Press, 240 pp

Grubb PLC (1971) Mineralogical anomalies in the Darling Range bauxites at Jarrahdale, Western Australia. Econ Geol 66: 1005–1016

Gualtieri AF, Venturelli P (1999) In situ study of the goethite-hematite phase transformation by real-time synchrotron powder diffraction. Am Mineral 84: 895–904

Haas JL Jr, Fisher JR (1976) Simultaneous evaluation and correlation of thermodynamic data. Am J Sci 276: 525–545

King EG (1955) Heat capacities at low temperatures and entropies at 298.16 K of crystalline calcium and magnesium aluminates. J Phys Chem 59: 218–219

Larson AC, von Dreele RB (1994) GSAS. General structure analysis system. LANSCE, MS-H805, Los Alamos, New Mexico

Liebermann RC, Maasch KA (1986) Acoustic and static compression experiments on the elastic behavior of hematite. J Geophys Res B 91: 4651–4656

Liu RA, Yund J, Tullis L, Topor, L, Navrotsky A (1995) Energy associated with dislocations: a calorimetric study using synthetic quartz. Phys Chem Miner 22: 67–73

MacKenzie KJD, Berezowski RM (1984) Thermal and Mössbauer studies of iron-containing hydrous silicates, V. Berthierine. Thermochim Acta 74: 291–312

Mongelli G, Acquafredda P (1999) Ferruginous concretions in a Late Cretaceous karst bauxite: composition and conditions of formation. Chem Geol 158: 315–320

Muan A, Gee CL (1956) Phase equilibrium studies in the system iron oxide–Al_2O_3 in air and at 1 atm O_2 pressure. J Am Ceram Soc 39: 207–214

Navrotsky A (1997) Progress and new directions in high-temperature calorimetry revisited. Phys Chem Miner 24: 222–241

Polli AD, Lange FF, Levi CG (1996) Crystallization behavior and microstructure evolution of $(Al,Fe)_2O_3$ synthesized from liquid precursors. J Am Ceram Soc 79: 1745–1755

Robie RA, Hemingway BS (1995) Thermodynamic properties of minerals and related substances at 298.15 K and 1 bar (10^5 pascals) and at higher temperatures. US Geol Surv Bull 2131, 461 pp

Schwertmann U, Cornell RM (2000) Iron oxides in the laboratory, 2nd edn. Wiley-VCH, Weinheim, 137 pp

Schwertmann U, Fitzpatrick RW, Taylor RM, Lewis DG (1979) The influence of aluminum on iron oxides, part II. Preparation and properties of Al-substituted hematites. Clays Clay Miner 27: 105–112

Stoffregen, RE, Alpers CN, Jambor JL (2000) Alunite-jarosite crystallography, thermodynamics, and geochronology. In:

Alpers CN, Jambor JL, Nordstrom DK (eds) Sulfate minerals. Rev Miner Geoch 40, 454–479

Stott FH, Chuah KT, Bradley LB (1998) Oxidation-sulphidation of iron aluminides. In: Grabke HJ, Schütze M (eds) Oxidation of Intermetallics. Wiley-VCH, 221–231

Van San E, De Grave E, Vandenberghe RE, Desseyn HO, Datas L, Barron V, Rousset A (2001) Study of Al-substituted hematites, prepared from thermal treatment of lepidocrocite. Phys Chem Miner 28: 488–497

Walker JS, Straguzzi GI, Manogue WH, Schuit GCA (1988) Carbon monoxide and propene oxidation by iron oxides for auto-emission control. J Catal 110: 298–309

Wells MA, Gilkes RJ, Anand RR (1989) The formation of corundum and aluminous hematite by the thermal dexydroxylation of aluminous goethite. Clay Miner 24: 513–530

Wells MA, Gilkes RJ, Fitzpatrick RW (2001) Properties and acid dissolution of metal-substituted hematites. Clays Clay Miner 49: 60–72

Willey RJ, Lai H, Peri JB (1991) Investigation of iron oxide-chromia-alumina aerogels for the selective catalytic reduction of nitric oxide by ammonia. J Catal 130: 319–331

Winkler B, Dove MT, Leslie M (1991) Static lattice energy minimization and lattice dynamics calculations on aluminosilicate minerals. Am Mineral 76: 313–331